


Ultrafast switching of persistent electron and hole ring currents in a molecule

Tennessee Joyce and Agnieszka Jaron

JILA and Department of Physics, University of Colorado, Boulder, Colorado-80309, USA (Received 19 April 2023; revised 27 September 2023; accepted 28 September 2023; published 16 November 2023)

A circularly polarized laser pulse can induce persistent intramolecular currents by either exciting or ionizing molecules. These two cases are identified as electron currents and hole currents, respectively, and up to now they have been studied only separately. We report *ab initio* time-dependent density-functional theory (TDDFT) simulations of currents in a molecule, which reveal for the first time that both electron and hole currents can be present simultaneously. By adjusting the intensity of the laser pulse, the balance between the two types of current can be controlled and the overall sign of the current can be switched. We provide a physical explanation for the effect in terms of molecular orbitals, which is consistent with the TDDFT simulations.

DOI: [10.1103/PhysRevA.108.053114](https://doi.org/10.1103/PhysRevA.108.053114)**I. INTRODUCTION**

It has long been understood that, in response to an applied magnetic field, the delocalized electrons of an aromatic molecule circulate in a so-called aromatic ring current [1,2]. This effect is important in nuclear magnetic resonance spectroscopy, where the internal magnetic field generated by the ring current is responsible for diamagnetic shielding [3]. In 2006, it was proposed that ring currents in molecules could also be induced by ultrashort UV laser pulses with circular or elliptical polarization [4,5]. The basic mechanism is that angular momentum carried by light is transferred to electrons in a molecule, causing them to circulate. By conservation of angular momentum, the current will persist after the pulse has ended (even without an external magnetic field) until the angular momentum dissipates somehow. Various experiments on atomic targets have confirmed the existence of the effect [6,7], although no direct observational data are available in the case of molecules. More recent interest in photoinduced ring currents [8–10] was motivated by the rapid technological advances in polarization control of high-harmonic radiation made in the last few years [11–13], which may enable experimental study of these phenomena in the near future [14].

There are at least three main advantages of photoinduced ring currents compared to the static magnetic field approach: first, the current is orders of magnitude stronger, and so is the internal magnetic field [15]; second, it enables femtosecond (or even attosecond) time-resolved studies of aromaticity and magnetism [16–18]; third, it establishes the possibility for coherent control of ring currents [19], which may have applications for controlling chemical reactions or the operation of advanced optoelectronic devices. This article will focus on the aspects related to the possibility of coherent control of the dynamics. In particular, we predict that, at high intensities of the driving laser, the charge carrier of the ring current transitions from electrons to holes (i.e., a sign change). This is interpreted as a control scheme, whereby the character of the ring current can be switched by varying the intensity of the laser pulse. This effect cannot be accounted for in the commonly used few-level model for ring currents, for reasons we discuss below, and therefore a more robust theoretical method

is required. For that reason, we use a series of *ab initio* time-dependent density functional theory (TDDFT) simulations to illustrate our control scheme in the case of benzene (C_6H_6), which is the prototypical aromatic molecule.

The two types of ring current mentioned above (electron and hole current) are usually studied separately in the literature. The distinction is essentially whether the ring current state was prepared through excitation or ionization. When the laser pulse excites the molecule into a state with nonvanishing current density, it is an electron current. When the laser pulse ionizes a molecule into a cationic state with nonvanishing current density (i.e., helicity-dependent ionization [20–23]), it is a hole current. Our main observation is that, in the interaction of atoms and molecules with strong laser fields, excitation and ionization (and therefore electron and hole currents) are often closely related and typically occur together. A typical example is resonance-enhanced multiphoton ionization (REMPI) [24,25], a two-step ionization process wherein an atom or molecule is first excited to an intermediate state (that must be resonant with some multiple of the laser frequency) and then subsequently ionized. Presently, we show that the balance between the electron and hole current during resonance-enhanced two-photon ionization of benzene leads to complex, but controllable, dynamics. We also demonstrate that because the few-level model neglects ionization completely, it is unable to account for this effect.

This article is structured as follows. We begin by reviewing theoretical and numerical methods, TDDFT in Sec. II A, and the few-level model in Sec. II B. Next we present our results, with the charge and current densities in Sec. III A, the occupations of molecular orbitals in Sec. III B, and the dependence on molecular orientation in Sec. III C. We finish with a conclusion in Sec. IV.

II. METHODS**A. Time-dependent density functional theory**

Our main theoretical method is TDDFT, as implemented by OCTOPUS [26–28]. We solve the time-dependent Kohn-Sham equations (using atomic units $\hbar = e = m_e = 4\pi\epsilon_0 = 1$

throughout)

$$i \frac{d}{dt} \psi_n(\mathbf{r}, t) = \left[-\frac{1}{2} \nabla^2 + V(\mathbf{r}, t) + \mathbf{r} \cdot \mathcal{E}(t) \right] \psi_n(\mathbf{r}, t), \quad (1)$$

for the 30 valence electrons (distributed into 15 doubly occupied orbitals ψ_n in order of increasing energy), while the 12 core electrons are modeled by pseudopotentials [29]. The time-dependent Kohn-Sham potential $V(\mathbf{r}, t)$ is approximated using the Perdew-Zunger parametrization of the local density approximation [30] with the self-interaction correction implemented with the optimized effective potential formalism [31]. Note that the self-interaction correction ensures the correct long-range behavior $V(\mathbf{r}, t) \rightarrow -1/r$ and is crucial for simulating ionization. The laser pulse is described in the dipole approximation by the following electric field

$$\mathcal{E}(t) = \begin{cases} \mathcal{E} \sin^2(\pi t/T) \text{Re}[\hat{\epsilon} e^{i\omega(t-T/2)}], & 0 < t < T, \\ 0, & \text{otherwise,} \end{cases} \quad (2)$$

with central frequency $\omega = 6.76 \text{ eV}$ (183 nm, resonant with the E_{1u} state as computed with linear response TDDFT, see below), duration $T = 16\pi/\omega = 202 \text{ a.u.} = 4.9 \text{ fs}$ (eight optical cycles), circular polarization $\hat{\epsilon} = (\hat{x} + i\hat{y})/\sqrt{2}$ (with the molecule in the xy plane), and a variable peak amplitude \mathcal{E} ranging up to 0.01687 a.u. (corresponding to maximum intensity of 10^{13} W/cm^2). The nuclei are fixed at bond lengths $|\text{CC}| = 1.39 \text{ \AA}$ and $|\text{CH}| = 1.09 \text{ \AA}$ with the six-fold symmetry enforced exactly. We verify that moving the nuclei according to Ehrenfest molecular dynamics does not significantly affect the results due to the very short pulse duration. Equation (1) is propagated from $t = 0$ up to $t = 2T = 404 \text{ a.u.}$ with the Crank-Nicolson method with a grid spacing of $dx = 0.4 \text{ a.u.}$ and a time step of 0.1 a.u. The simulation box has the so-called minimum box shape, which is the union of balls of radii 25 a.u. centered at each atom. The outermost 10 a.u. in each direction is used for a complex absorbing potential.

Once the time-dependent Kohn-Sham orbitals are known, we can compute the time-dependent charge and current densities using

$$\rho(\mathbf{r}, t) = 2 \sum_{n=1}^{15} |\psi_n(\mathbf{r}, t)|^2, \quad (3)$$

$$\mathbf{J}(\mathbf{r}, t) = 2 \sum_{n=1}^{15} \text{Im}[\psi_n^*(\mathbf{r}, t) \nabla \psi_n(\mathbf{r}, t)]. \quad (4)$$

In addition to the full time-dependent simulations, we also used the Casida formulation of linear response TDDFT [32] to compute information about the E_{1u} excited state. The numerical parameters were the same as above except with a smaller radius of 10 a.u. for the minimum box shape, and no absorbing boundary (because we are only computing a bound state). Interestingly, we found that a large number of unoccupied orbitals (160) were required to converge this excited state. Those high-lying orbitals have a maximum energy of 12 eV past the ionization threshold, which is just beyond the peak of the plasmon resonance in the photoionization cross section [33], suggesting electron correlation mixes the bound state with that resonance structure. This can be quantified by examining the orbital contributions to the E_{1u} excited state in

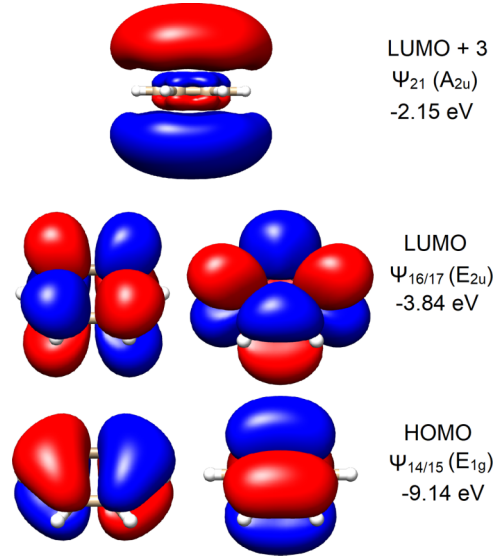


FIG. 1. Kohn-Sham orbitals which participate in the E_{1u} excited state in benzene, their symmetries and energies (in a.u.). Both HOMO and LUMO are doubly degenerate, while LUMO + 3 is not.

the form of occupied-unoccupied pairs:

- (1) 68% HOMO \rightarrow LUMO;
- (2) 26% HOMO \rightarrow LUMO + 3;
- (3) 6% other.

Although the dominant contribution goes between the doubly degenerate highest occupied molecular orbitals (HOMO ψ_{14} and ψ_{15}) and doubly degenerate lowest unoccupied molecular orbitals (LUMO ψ_{16} and ψ_{17}), a significant percentage also goes to LUMO + 3 (ψ_{21}), and the remaining 6% is distributed among a large number of continuum orbitals, presumably corresponding to the plasmon resonance. We plot the relevant field-free Kohn-Sham orbitals in Fig. 1. Since all of these orbitals lie above and below the plane of the molecule, we expect that most of the dynamics also happens outside the plane of molecule.

B. Few-level model

First we consider the commonly used few-level model of ring currents. In this model, the wave function is approximated as a linear combination of a small number of electronic states $|\Psi_j\rangle$ with energy eigenvalues E_j ,

$$|\Psi(t)\rangle = \sum_j c_j(t) e^{-iE_j t} |\Psi_j\rangle. \quad (5)$$

We emphasize the distinction between the Kohn-Sham orbitals $\psi_n(\mathbf{r})$, which are single-electron wave functions and the multielectron eigenstates $|\Psi_j\rangle$. We assume without loss of generality that the wave functions associated with $|\Psi_j\rangle$ are real-valued. The interaction of the molecule with a laser pulse is modeled by the time-dependent Schrödinger equation in the interaction picture

$$i \frac{\partial c_j(t)}{\partial t} = \sum_k c_k(t) \mathcal{E}(t) \mu_{jk} e^{i(E_j - E_k)t}, \quad (6)$$

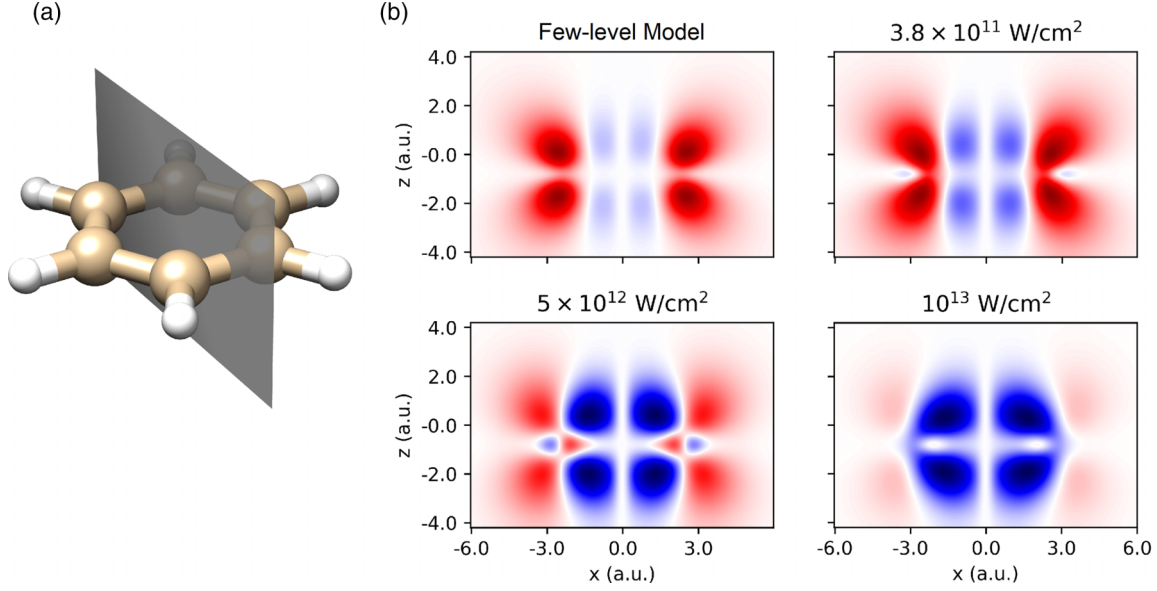


FIG. 2. (a) Taking a cross section through the molecule of the current density. To make the result independent of how the cross section is taken, we average over all possible orientations of the plane [see Eq. (11)]. (b) Angle-averaged cross sections of the persistent ring current induced in a benzene molecule by laser pulses with different peak intensities. At low intensity the electron current (red) dominates, while at high intensity the hole current (blue) dominates. The shape of the current (above and below the plane) is consistent with the HOMO and LUMO orbitals from Fig. 6, and we note that the ring of carbon atoms at $x = \pm 2.63$ a.u. and the ring of hydrogen atoms is at $x = \pm 4.69$ a.u..

where μ_{jk} is the transition dipole between $|\Psi_j\rangle$ and $|\Psi_k\rangle$. Finally, the time-dependent charge and current densities can be computed using the following expressions:

$$\rho(\mathbf{r}, t) = 2 \sum_{j < k} \text{Re}[c_j^*(t)c_k(t)e^{-i(E_k - E_j)t}] \rho_{jk}(\mathbf{r}), \quad (7)$$

$$\mathbf{J}(\mathbf{r}, t) = 2 \sum_{j < k} \text{Im}[c_j^*(t)c_k(t)e^{-i(E_k - E_j)t}] \mathbf{J}_{jk}(\mathbf{r}), \quad (8)$$

where

$$\rho_{jk}(\mathbf{r}) = \langle \Psi_j | \hat{\rho}(\mathbf{r}) | \Psi_k \rangle, \quad (9)$$

$$\mathbf{J}_{jk}(\mathbf{r}) = i \langle \Psi_j | \hat{\mathbf{J}}(\mathbf{r}) | \Psi_k \rangle, \quad (10)$$

$\hat{\rho}(\mathbf{r})$ and $\hat{\mathbf{J}}(\mathbf{r})$ are the usual charge and current density operators. Note because we use a real-valued eigenbasis, time-reversal symmetry implies ρ_{jk} and \mathbf{J}_{jk} are real symmetric and antisymmetric matrices, respectively, which leads to Eqs. (7) and (8).

After the laser pulse ends the $c_j(t)$ remain constant but most terms in Eqs. (7) and (8) continue to oscillate with frequencies corresponding to the energy differences between states; this is an example of attosecond charge migration [34]. However, when two electronic states are degenerate $E_j = E_k$ those terms will not oscillate. Those degenerate terms produce persistent ring currents which are divergenceless, and therefore do not correspond to any net motion of the charge density (i.e., it can be shown that $\nabla \cdot \mathbf{J}_{jk} = 0$ whenever $E_j = E_k$).

For benzene, we include three electronic states: the A_{1g} ground state $|\Psi_0\rangle$ and the doubly degenerate E_{1u} excited states $|\Psi_1\rangle$ and $|\Psi_2\rangle$ which were discussed in Sec. II A. The model parameters E_j and μ_{jk} were computed using linear response TDDFT as described in that section and the charge and current

densities ρ_{jk} and \mathbf{J}_{jk} were estimated using an extension of the linear response formalism derived in Appendix A.

III. RESULTS

A. Charge and current densities

We begin by visualizing the charge and current densities produced by both theoretical models. As discussed around Eqs. (7) and (8), these densities contain both stationary and oscillatory components.

The stationary component of the current density is best visualized by computing an angle-averaged cross section defined by the following integral [in cylindrical coordinates (ρ, z, ϕ)]

$$J(x, z, t) = \frac{1}{2\pi} \int_0^{2\pi} \hat{\phi} \cdot \mathbf{J}(|x|, z, \phi) d\phi. \quad (11)$$

As illustrated in Fig. 2(a), we take the component of the current passing through a plane, then average over all orientation angles ϕ of that plane. In the two-level model, the cross-sectional current is constant for $t > T$, while in the full TDDFT simulation that is only approximately true. These integrated current densities are plotted in Fig. 2(b) at time $t = 200$ a.u. $\approx T$ for several peak laser intensities, as well as for the few-level model (for which the shape is independent of laser intensity). The red parts of the current are corotating with the laser field, while the blue parts are counterrotating. Within each subplot the color scale is relative to the maximum absolute value of the current density in that subplot because the magnitude of the current increases rapidly with intensity, even though the shape only changes gradually. At low intensities the current is a combination of a strong electron current (red) and a weak hole current (blue), while at high intensities the

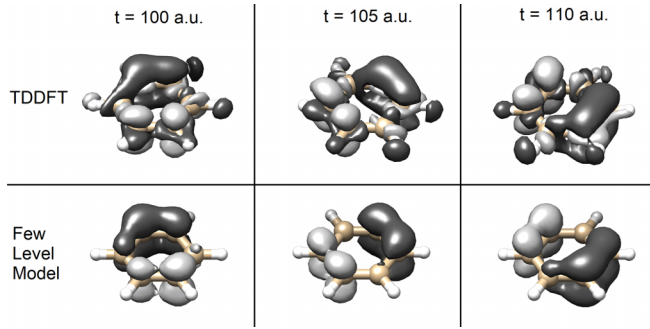


FIG. 3. Motion of charge density around the molecule near the peak of the laser pulse, for both TDDFT and the few-level model. Light areas are excess electrons (compared to the ground-state charge distribution) while dark areas are holes. For both models, the cloud of displaced charge circulates around the molecule with a period of 612 as, corresponding to the energy of the E_{1u} excited state (which is also the laser frequency). The peak laser intensity is 5×10^{12} W/cm².

electron current disappears so that the hole current dominates. The reason for this is explained in Sec. III B.

The oscillatory part, on the other hand, is best visualized by plotting isosurfaces of the density difference

$$\Delta\rho(\mathbf{r}, t) = \rho(\mathbf{r}, t) - \rho(\mathbf{r}, 0) \quad (12)$$

(with isovalues $\pm 2 \times 10^{-3}$ a.u.) at several points in time. Figure 3 shows snapshots of the density difference near the peak of the laser pulse ($t \approx 0.5T$), while Fig. 4 shows snapshots long after the pulse ends ($t \approx 2T$), both for a peak laser intensity of 5×10^{12} W/cm². The light areas indicate excess electrons ($\Delta\rho > 0$) while the dark areas indicate holes ($\Delta\rho < 0$).

During the laser pulse (Fig. 3) the two models agree very well, although TDDFT predicts additional involvement of the hydrogen atoms. For both models, the cloud of displaced charge circulates around the molecule with a period of (612 as), which is both the laser frequency and the energy of the excited state. After the laser pulse (Fig. 4) the shape of the

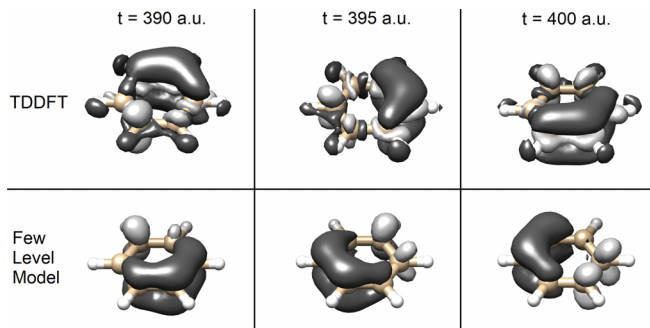


FIG. 4. Same as Fig. 3 except long after the pulse ends. The charge continues to move around because the molecule is in a superposition of multiple electronic states (here mostly the ground A_{1g} state and the excited E_{1u} states). The two models gradually become out of sync because the energy of the states within TDDFT is not necessarily the same as the field-free energies. Nevertheless, the shape of the displaced charge is remarkably similar between the two models.

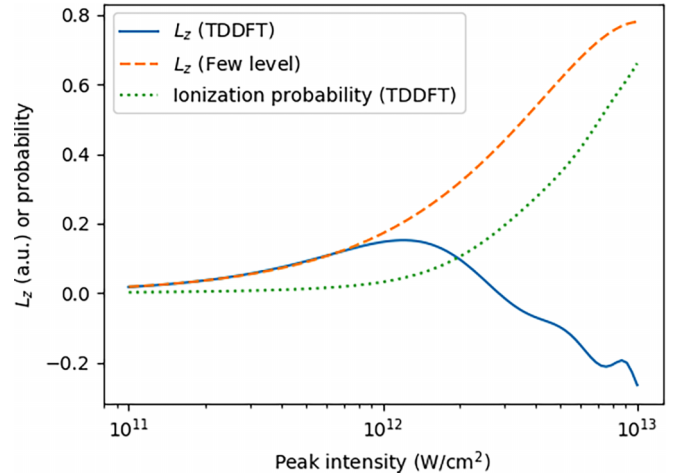


FIG. 5. Comparison of full TDDFT simulations (solid blue line) to the commonly used few-level model for ring currents (orange dashed line). At low intensity (below 10^{12} W/cm²) the two models agree, but the few-level model is unable to explain the reversal at high intensity. Because the ionization probability (dotted green line) becomes significant around the same time as the reversal, these data support our proposed explanation that resonant enhanced two-photon ionization is responsible for the switch from electron to hole current.

charge density is similar for both models, but there appears to be a phase offset between them. This suggests that the energy of the excited state drifts slightly in the TDDFT model, which gradually modifies the relative phase.

Another important observation about the density difference is that the dark areas are generally larger than the light areas. In the TDDFT model this indicates ionization. Strangely, the few-level model also appears to have larger dark areas than light areas even though it does not include ionization, and in fact, the density difference must integrate to zero. This is actually caused by excitation to LUMO + 3 which is very diffuse (see Fig. 1) and so requires a much lower isovalue to see. Therefore the excess of darker areas in the TDDFT model is also likely a combination of both ionization and excitation to diffuse orbitals (see Sec. III B and Fig. 7 for a more quantitative answer).

The intensity dependence of these dynamics is illustrated in Fig. 5. Here, the current is summarized by computing the z component of the magnetic moment (or equivalently, the z component of the electronic angular momentum)

$$L_z(t) = \int (-y\hat{x} + x\hat{y})\mathbf{J}(\mathbf{r}, t)d^3\mathbf{r}. \quad (13)$$

Since the domain of integration is the simulation box, ionized electrons are not included. For this reason we plot $L_z(2T)$ so that the ionizing wavepacket has plenty of time to leave the box. The results are interpolated over intensity to obtain a smooth curve using the method discussed in Appendix B. Whereas in the few-level model the magnetic moment increases monotonically with the laser intensity (up to about 10^{13} W/cm², after which the system Rabi oscillates back to the ground state), in TDDFT the current starts to decrease already around 10^{12} W/cm², and eventually reverses sign shortly after. We also plot the total ionization probability and

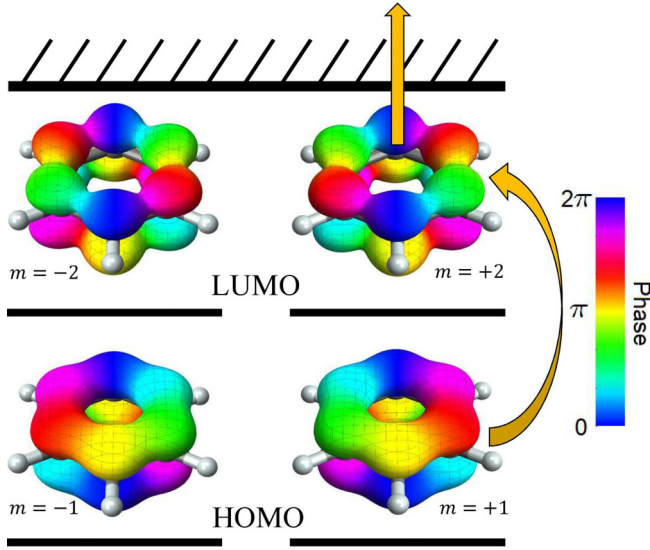


FIG. 6. Schematic explaining the transition from electron to hole current in terms of resonant two-photon ionization. First, an electron is excited from HOMO to LUMO (and by selection rules for circularly polarized light, this must be from $m = +1$ to $m = +2$). The excited electron in LUMO circulates in a persistent current, but the hole left behind in HOMO also contributes a (weaker) current with opposite sign. At sufficiently high laser intensity, the excited LUMO electron may absorb a second photon and ionize. This leaves behind only the hole current and explains the sign change as a function of intensity.

can from this conclude that the reversal occurs precisely when the ionization probability becomes significant.

B. Explanation using complex orbitals

The results presented so far can be understood qualitatively in terms of complex molecular orbitals, as illustrated schematically in Fig. 6. This simply involves a change of basis from the real-valued orbitals shown earlier in Fig. 1

$$\psi_{\pm}^{\text{HOMO}}(\mathbf{r}) = [\psi_{14}(\mathbf{r}) \pm \psi_{15}(\mathbf{r})]/\sqrt{2}, \quad (14)$$

$$\psi_{\pm}^{\text{LUMO}}(\mathbf{r}) = [\psi_{16}(\mathbf{r}) \pm \psi_{17}(\mathbf{r})]/\sqrt{2}, \quad (15)$$

where the color in Fig. 6 indicates the complex phase. The advantage of using complex orbitals is that they are eigenfunctions of the six-fold symmetry operator (rotation about the molecular axis by 60°)

$$\exp\left[-\frac{i\pi}{3}\hat{L}_z\right]\psi_{\pm}^{\text{HOMO}}(\mathbf{r}) = \exp\left[\mp\frac{i\pi}{3}\right]\psi_{\pm}^{\text{HOMO}}(\mathbf{r}), \quad (16)$$

$$\exp\left[-\frac{i\pi}{3}\hat{L}_z\right]\psi_{\pm}^{\text{LUMO}}(\mathbf{r}) = \exp\left[\mp\frac{2i\pi}{3}\right]\psi_{\pm}^{\text{LUMO}}(\mathbf{r}). \quad (17)$$

In other words, the complex orbitals have magnetic quantum numbers m defined modulo 6: ψ_{\pm}^{HOMO} have $m = \pm 1$ and ψ_{\pm}^{LUMO} have $m = \pm 2$. Just as for atomic orbitals, the sign of m indicates the direction the electron circulates around the molecule, and the magnitude indicates more-or-less the angular speed. We chose our conventions such that $m > 0$ electrons are corotating with the laser field and $m < 0$ electrons are counterrotating.

Using this notation, we can now give the qualitative explanation illustrated in Fig. 6. In the ground state, both ψ_{\pm}^{HOMO} are doubly occupied, so there is zero net current. When the benzene molecule is exposed to a circularly polarized laser pulse, the usual selection rule $\Delta m = 1$ applies (we assume for now that the molecules are oriented such that the laser is polarized in the molecular plane, see Sec. III C for the more general case), so that the only dipole-allowed transition is ψ_{+}^{HOMO} to ψ_{+}^{LUMO} , which is the dominant component of the E_{1u} excited state discussed in Sec. II A. The electron excited to LUMO contributes a strong corotating current ($m = +2$), but the imbalance of electrons in the HOMO contributes a weaker counterrotating current ($m = -1$). This can alternatively be interpreted as a positively charged hole occupying ψ_{+}^{HOMO} producing a corotating hole current (rather than a counterrotating electron current). This is precisely what we see in the top row of Fig. 2(b), two components to the current with opposite sign (red and blue).

To explain the reversal of the current at higher intensity [bottom row of Fig. 2(b)], we simply recognize that the electron previously excited to ψ_{+}^{LUMO} can absorb a second photon from the same laser pulse, ionizing and leaving behind only the hole current. The balance between the one-photon excitation and the two-photon ionization processes can be controlled by varying the laser intensity because the first scales with I while the second scales with I^2 . Furthermore, it is apparent that this sign reversal can be interpreted as a change in the dominant charge carrier from electrons to holes.

To further validate the qualitative model, we compute the distribution of final states for the HOMO electrons by projecting onto the field-free orbitals

$$P_{\pm \rightarrow n} = \left| \int \psi_n^*(\mathbf{r}, 0) \left[\frac{\psi_{14}(\mathbf{r}, 2T) \pm i\psi_{15}(\mathbf{r}, 2T)}{\sqrt{2}} \right] d^3\mathbf{r} \right|^2, \quad (18)$$

$$P_{\pm}^{\text{ionize}} = 1 - \int \left| \frac{\psi_{14}(\mathbf{r}, 2T) \pm i\psi_{15}(\mathbf{r}, 2T)}{\sqrt{2}} \right|^2 d^3\mathbf{r}. \quad (19)$$

Here $P_{\pm \rightarrow n}$ should be thought of as the probability for the electron that began in ψ_{\pm}^{HOMO} to end up in ψ_n and P_{\pm}^{ionize} should be thought of as the probability for that electron to be ionized (i.e., leave the simulation box). Since the ψ_n are a complete basis inside the simulation box, these probabilities add up to 1 if enough unoccupied orbitals are included. We emphasize that the probabilities are not physically observable because they describe the artificial noninteracting Kohn-Sham system. Nonetheless, this sort of analysis can be used to gain some intuition about the physical mechanisms at work.

Results for the final state probabilities are plotted in Fig. 7 as a function of the laser intensity. On the left is the corotating electron ($P_{+ \rightarrow n}$ and P_{+}^{ionize}) while on the right is the counterrotating electron ($P_{- \rightarrow n}$ and P_{-}^{ionize}). The probabilities for HOMO and LUMO are grouped together (i.e., $[P_{+ \rightarrow 14} + P_{+ \rightarrow 15}]$ and $[P_{+ \rightarrow 16} + P_{+ \rightarrow 17}]$, respectively), and the “other” line is the remaining probability such that the four lines in each plot sum to 1. These results are consistent with the qualitative explanation we proposed: the corotating can either be excited or ionized and the relative probability of the two outcomes can be controlled with the laser intensity. Interestingly, the excitation probability appear to saturate around

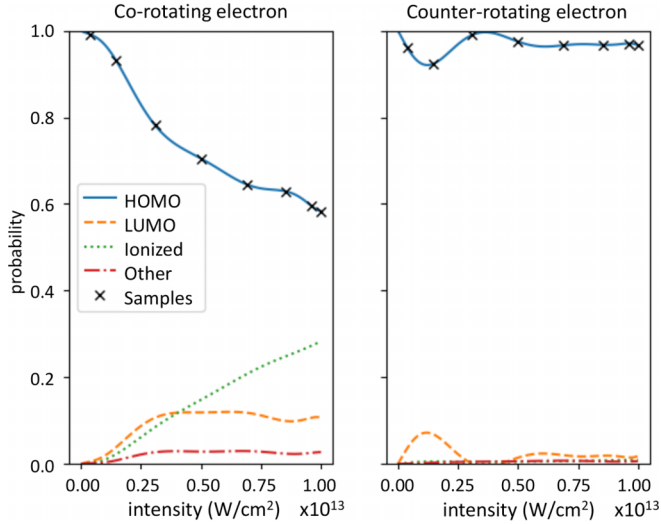


FIG. 7. Final-state probabilities of the co and counterrotating HOMO electrons as a function of the laser intensity, from the TDDFT simulations. The blue solid line is the probability for the HOMO electron to end in either of the two HOMO orbitals, the yellow dashed line is the probability to end in either of the two LUMO orbitals, the green dotted line is the ionization probability for that electron, and the red dash-dotted line is the remaining probability so that the total is one. This last category includes excitation to other orbitals, as well as the part of the outgoing wavepacket which has not left the box yet.

$3 \times 10^{12} \text{ W/cm}^2$ while the ionization probability continues to increase. The counterrotating electron, on the other hand, has a very low ionization probability because it is not resonance-enhanced. That electron is excited with some probability to LUMO + 3, as we expect from the linear response calculation (since LUMO + 3 has $m = 0$, selection rules imply that only the counterrotating electron can excited into it).

C. Orientation dependence

In a real experiment, it may not be possible or convenient to align the molecules as we have so far assumed. To shed light on this situation, we repeated the highest intensity TDDFT calculation (10^{13} W/cm^2) several values of the alignment angle $\theta = 0, 22.5^\circ, 45^\circ, 67.5^\circ$ by using $\hat{\epsilon} = (\cos\theta\hat{x} + i\hat{y} + \sin\theta\hat{z})/\sqrt{2}$ in Eq. (2). Symmetry and periodicity imply that the θ dependence can be expanded in a Fourier series of the form

$$L_z(t, \theta) = \sum_{n=0}^{\infty} L_z^{(n)}(t) \cos[(2n+1)\theta]. \quad (20)$$

We truncate this sum at four terms and solve for the coefficients $L_z^{(n)}$ to approximate L_z as a smooth function of θ . The results of these calculations are shown in Fig. 8 for two different laser intensities: $1.47 \times 10^{12} \text{ W/cm}^2$ (before reversal) and 10^{13} W/cm^2 (after reversal). At the lower intensity, the current is very robust to molecular orientation, essentially unchanged up to 45° misalignment. At high intensity, the final magnitude of the current depends more sensitively on alignment, but the sign is uniformly negative, that is, the reversal always occurs at high intensity no matter the orientation. Therefore,

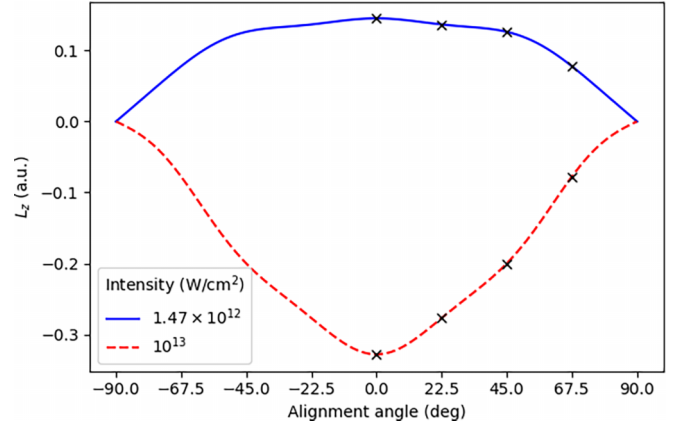


FIG. 8. Orientation dependence of the induced magnetic moment (in the molecular frame) long after the end of the laser pulse ($t = 2T$). At low laser intensity, the magnetic moment is relatively flat even out to 45° misalignment. At higher intensity, the strength of the magnetic moment is somewhat more sensitive to the orientation, but the sign is not. That is, the reversal of the current occurs for any orientation. The black x's mark the sampled angles for which we ran the simulation, and the lines are interpolated between those data points using Eq. (20).

the reversal we predicted will still be observable under typical experimental conditions even without aligning the molecules.

IV. CONCLUSION

In conclusion, we showed that both electron and hole currents are present during resonance-enhanced two-photon ionization of benzene. This enables a control scheme, wherein the balance of the two types of currents is controlled by varying the laser intensity. We proposed a simple qualitative description for the effect in terms of molecular orbitals, which was consistent with the results of full TDDFT simulations. Our results also suggest that the few-level model typically used to study photoinduced ring currents may be insufficient even for moderate laser intensities around 10^{12} W/cm^2 . Lastly, we showed that the effect and the control scheme are robust with respect to the orientation of the molecules, making it more practical to implement in realistic experimental conditions.

ACKNOWLEDGMENTS

This work was supported by the NSF (Awards No. PHY-1734006 and No. PHY-2110628) This work utilized resources from the University of Colorado Boulder Research Computing Group, which is supported by the National Science Foundation (Awards No. ACI-1532235 and No. ACI-1532236), the University of Colorado Boulder, and Colorado State University.

APPENDIX A: LINEAR RESPONSE TDDFT

In this Appendix we propose a simple method to estimate the matrix elements for charge and current density

ρ_{jk} and \mathbf{J}_{jk} [defined in Eqs. (7) and (8)] from the Casida formulation of linear response TDDFT [32]. Although this task goes beyond the range of validity of linear response when both $|\Psi_j\rangle$ and $|\Psi_k\rangle$ are excited states (because the observable is then quadratic in the field strength), we would argue that the method at least provides a well-defined prescription for approximating these quantities. Furthermore, the results presented in the text (Figs. 2 to 5) suggest that this approach agrees fairly well with the full TDDFT calculations at low intensities and that at higher intensities the discrepancy is more due to the inability of the few-level model to describe ionization rather than a problem with the matrix elements for charge and current density.

The solution to Casida's equation essentially produces a multielectron wave function for each excited state, expanded in the basis of occupied-unoccupied orbital pairs, which can be understood to approximate the exact multielectron wave function in the same sense that the Slater determinant of the Kohn-Sham orbitals approximates the exact multielectron ground state. We use fermion creation and annihilation operators $a_{u\sigma}^\dagger, a_{o\sigma}$ where o ranges over all occupied orbitals ($o = 1, \dots, 15$), u ranges over all unoccupied orbitals ($u = 16, \dots, 175$), and $\sigma = \uparrow, \downarrow$ is the spin index. In that notation, the multielectron wave function for the j th excited state is approximated by

$$|\Psi_j\rangle \approx |\Psi_j^{\text{Cas}}\rangle = \frac{1}{\sqrt{2}} \sum_{o,u,\sigma} c_{jou} \hat{a}_{u\sigma}^\dagger \hat{a}_{o\sigma} |\Psi_0^{\text{KS}}\rangle, \quad (\text{A1})$$

where c_{jou} are the coefficients determined from Casida's equation

$$|\Psi_0^{\text{KS}}\rangle = \left(\prod_{o,\sigma} a_{o\sigma}^\dagger \right) |0\rangle, \quad (\text{A2})$$

is the Kohn-Sham ground state, and $|0\rangle$ is the vacuum state (no electrons). Any spin-independent one-body operator can be represented in the basis of Kohn-Sham orbitals as

$$\hat{O} = \sum_{m\sigma} O_{mn}^{1B} \hat{a}_{m\sigma}^\dagger \hat{a}_{n\sigma}. \quad (\text{A3})$$

Applying commutation relations, the matrix element between two excited states is

$$\begin{aligned} \langle \Psi_j | \hat{O} | \Psi_k \rangle &= \sum_{o,u,u'} c_{jou} c_{kou'} O_{uu'}^{1B} - \sum_{o,\sigma,u} c_{jou} c_{k\sigma u} O_{o\sigma}^{1B} \\ &\quad + 2\delta_{jk} \sum_o O_{oo}^{1B}, \end{aligned} \quad (\text{A4})$$

and between the ground state and an excited state is

$$\langle \Psi_0 | \hat{O} | \Psi_j \rangle = \sqrt{2} \sum_{o,u} c_{jou} O_{ou}^{1B}.$$

The one-body matrices for the charge and current densities are

$$\rho_{mn}^{1B}(\mathbf{r}) = \psi_m^*(\mathbf{r}) \psi_n(\mathbf{r}), \quad (\text{A5})$$

$$\mathbf{J}_{mn}^{1B}(\mathbf{r}) = \frac{1}{2i} [\psi_m^*(\mathbf{r}) \nabla \psi_n(\mathbf{r}) - \psi_n(\mathbf{r}) \nabla \psi_m^*(\mathbf{r})]. \quad (\text{A6})$$

APPENDIX B: INTERPOLATION

In this section we describe the interpolation method used in the main text. Given some observable $f(\mathcal{E})$ that is a function of the peak electric field strength \mathcal{E} (with all other parameters fixed), we would like to approximate it by a smooth function on the interval $[0, \mathcal{E}_{\text{max}}]$ using as few sample values $f(\mathcal{E}_j)$ as possible. In all cases we considered, f is either an even or odd function of \mathcal{E} and the value of $f(0)$ is known, meaning we can extend the interval to $[-\mathcal{E}_{\text{max}}, \mathcal{E}_{\text{max}}]$ for free. Then a particularly efficient choice of sample field strengths is the Chebyshev nodes of the second kind

$$\mathcal{E}_j = \mathcal{E}_{\text{max}} \cos\left(\frac{j\pi}{2N}\right), \quad j = 0, \dots, 2N. \quad (\text{B1})$$

For the symmetry reasons discussed above, we only need to evaluate $f(\mathcal{E}_j)$ at the first N field strengths (which have $\mathcal{E}_j > 0$) to obtain the function value at the remaining $N + 1$ strengths.

Next, we interpolate a polynomial of degree $2N$ through the $2N + 1$ sample points. In barycentric form [35], that is,

$$f(\mathcal{E}) \approx \frac{\sum_{j=0}^{2N} w_j f(\mathcal{E}_j) (\mathcal{E} - \mathcal{E}_j)^{-1}}{\sum_{j=0}^{2N} w_j (\mathcal{E} - \mathcal{E}_j)^{-1}}, \quad (\text{B2})$$

where

$$w_j = \begin{cases} 0.5(-1)^j, & j = 0, 2N, \\ (-1)^j, & j = 1, \dots, 2N - 1. \end{cases} \quad (\text{B3})$$

[1] J. A. N. F. Gomes and R. B. Mallion, *Chem. Rev.* **101**, 1349 (2001).
[2] T. M. Krygowski, H. Szatyłowicz, O. A. Stasyuk, J. Dominikowska, and M. Palusiak, *Chem. Rev.* **114**, 6383 (2014).
[3] T. Heine, C. Corminboeuf, and G. Seifert, *Chem. Rev.* **105**, 3889 (2005).
[4] I. Barth and J. Manz, *Angew. Chem., Int. Ed.* **45**, 2962 (2006).
[5] I. Barth, J. Manz, Y. Shigeta, and K. Yagi, *J. Am. Chem. Soc.* **128**, 7043 (2006).
[6] M. Wollenhaupt, M. Krug, J. Köhler, T. Bayer, C. Sarpe-Tudoran, and T. Baumert, *Appl. Phys. B* **95**, 245 (2009).

[7] S. Eckart, M. Kunitski, M. Richter, A. Hartung, J. Rist, F. Trinter, K. Fehre, N. Schlott, K. Henrichs, L. P. H. Schmidt, T. Jahnke, M. Schöffler, K. Liu, I. Barth, J. Kaushal, F. Morales, M. Ivanov, O. Smirnova, and R. Dörner, *Nat. Phys.* **14**, 701 (2018).
[8] Q. Xu, Y. He, S. Yan, and J. Guo, *J. Phys. B: At. Mol. Opt. Phys.* **56**, 035401 (2023).
[9] S. Sun, H. Yong, F. Chen, and S. Mukamel, *Chem. Sci.* **13**, 10327 (2022).
[10] S. Giri, A. M. Dudzinski, J. C. Tremblay, and G. Dixit, *Phys. Rev. A* **102**, 063103 (2020).

- [11] A. Fleischer, O. Kfir, T. Diskin, P. Sidorenko, and O. Cohen, *Nat. Photonics* **8**, 543 (2014).
- [12] D. D. Hickstein, F. J. Dollar, P. Grychtol, J. L. Ellis, R. Knut, C. Hernandez-Garcia, D. Zusin, C. Gentry, J. M. Shaw, T. Fan, K. M. Dorney, A. Becker, A. Jaron-Becker, H. C. Kapteyn, M. M. Murnane, and C. G. Durfee, *Nat. Photonics* **9**, 743 (2015).
- [13] P.-C. Huang, C. Hernandez-Garcia, J.-T. Huang, P.-Y. Huang, C.-H. Lu, L. Rego, D. D. Hickstein, J. L. Ellis, A. Jaron-Becker, A. Becker, S.-D. Yang, C. G. Durfee, L. Plaja, H. C. Kapteyn, M. M. Murnane, A. H. Kung, and M.-C. Chen, *Nat. Photonics* **12**, 349 (2018).
- [14] O. Neufeld and O. Cohen, *Phys. Rev. Lett.* **123**, 103202 (2019).
- [15] K.-J. Yuan and A. D. Bandrauk, *Phys. Rev. A* **88**, 013417 (2013).
- [16] X. Zhang, X. Zhu, D. Wang, L. Li, X. Liu, Q. Liao, P. Lan, and P. Lu, *Phys. Rev. A* **99**, 013414 (2019).
- [17] I. S. Ulusoy and M. Nest, *J. Am. Chem. Soc.* **133**, 20230 (2011).
- [18] K.-J. Yuan, C.-C. Shu, D. Dong, and A. D. Bandrauk, *J. Phys. Chem. Lett.* **8**, 2229 (2017).
- [19] H. Mineo and Y. Fujimura, *J. Chem. Phys.* **147**, 224301 (2017).
- [20] I. Barth and O. Smirnova, *Phys. Rev. A* **84**, 063415 (2011).
- [21] T. Herath, L. Yan, S. K. Lee, and W. Li, *Phys. Rev. Lett.* **109**, 043004 (2012).
- [22] X. Zhu, P. Lan, K. Liu, Y. Li, X. Liu, Q. Zhang, I. Barth, and P. Lu, *Opt. Express* **24**, 4196 (2016).
- [23] K. Liu and I. Barth, *Phys. Rev. A* **94**, 043402 (2016).
- [24] V. S. Antonov, I. N. Knyazev, V. S. Letokhov, V. M. Matiuk, V. G. Movshev, and V. K. Potapov, *Opt. Lett.* **3**, 37 (1978).
- [25] W. Dietz, H. J. Neusser, U. Boesl, E. W. Schlag, and S. H. Lin, *Chem. Phys.* **66**, 105 (1982).
- [26] M. A. L. Marques, A. Castro, G. F. Bertsch, and A. Rubio, *Comput. Phys. Commun.* **151**, 60 (2003).
- [27] A. Castro, H. Appel, M. Oliveira, C. A. Rozzi, X. Andrade, F. Lorenzen, M. A. L. Marques, E. K. U. Gross, and A. Rubio, *Phys. Status Solidi B* **243**, 2465 (2006).
- [28] X. Andrade, D. Strubbe, U. D. Giovannini, A. H. Larsen, M. J. T. Oliveira, J. Alberdi-Rodriguez, A. Varas, I. Theophilou, N. Helbig, M. J. Verstraete, L. Stella, F. Nogueira, A. Aspuru-Guzik, A. Castro, M. A. L. Marques, and A. Rubio, *Phys. Chem. Chem. Phys.* **17**, 31371 (2015).
- [29] N. Troullier and J. L. Martins, *Phys. Rev. B* **43**, 1993 (1991).
- [30] J. P. Perdew and A. Zunger, *Phys. Rev. B* **23**, 5048 (1981).
- [31] J. B. Krieger, Y. Li, and G. J. Iafrate, *Phys. Rev. A* **46**, 5453 (1992).
- [32] M. E. Casida, in *Recent Advances in Density Functional Methods, Recent Advances in Computational Chemistry*, Vol. 1 (World Scientific, 1995), pp. 155–192.
- [33] A. V. Verkhovtsev, A. V. Korol, and A. V. Solov'yov, *J. Phys.: Conf. Ser.* **490**, 012159 (2014).
- [34] H. J. Wörner, C. A. Arrell, N. Banerji, A. Cannizzo, M. Chergui, A. K. Das, P. Hamm, U. Keller, P. M. Kraus, E. Liberatore, P. Lopez-Tarifa, M. Lucchini, M. Meuwly, C. Milne, J.-E. Moser, U. Rothlisberger, G. Smolentsev, J. Teuscher, J. A. van Bokhoven, and O. Wenger, *Struct. Dyn.* **4**, 061508 (2017).
- [35] J.-P. Berrut and L. N. Trefethen, *SIAM Rev.* **46**, 501 (2004).